A dynamic biomimetic model of the membrane-bound CD4-CD3-TCR complex during pMHC disengagement

Zachary A. Rollins,[1] Roland Faller,[1] and Steven C. George[2,*]
[1]Department of Chemical Engineering, University of California, Davis, Davis, California and [2]Department of Biomedical Engineering, University of California, Davis, Davis, California

ABSTRACT The coordinated (dis)engagement of the membrane-bound T cell receptor (TCR)-CD3-CD4 complex from the peptide-major histocompatibility complex (pMHC) is fundamental to TCR signal transduction and T cell effector function. As such, an atomic-scale understanding would not only enhance our basic understanding of the adaptive immune response but would also accelerate the rational design of TCRs for immunotherapy. In this study, we explore the impact of the CD4 coreceptor on the TCR-pMHC (dis)engagement by constructing a molecular-level biomimetic model of the CD3-TCR-pMHC and CD4-CD3-TCR-pMHC complexes within a lipid bilayer. After allowing the system complexes to equilibrate (engage), we use steered molecular dynamics to dissociate (disengage) the pMHC. We find that 1) the CD4 confines the pMHC closer to the T cell by 1.8 nm at equilibrium; 2) CD4 confinement shifts the TCR along the MHC binding groove engaging a different set of amino acids and enhancing the TCR-pMHC bond lifetime; 3) the CD4 translocates under load increasing the interaction strength between the CD4-pMHC, CD4-TCR, and CD4-CD3; and 4) upon dissociation, the CD3-TCR complex undergoes structural oscillation and increased energetic fluctuation between the CD3-TCR and CD3-lipids. These atomic-level simulations provide mechanistic insight on how the CD4 coreceptor impacts TCR-pMHC (dis)engagement. More specifically, our results provide further support (enhanced bond lifetime) for a force-dependent kinetic proofreading model and identify an alternate set of amino acids in the TCR that dominate the TCR-pMHC interaction and could thus impact the design of TCRs for immunotherapy.

SIGNIFICANCE The (dis)engagement of the membrane-bound T cell receptor determines T cell effector function and depends on several coreceptor interactions including the CD3 and CD4. The ability to design T cell receptors will be advanced by understanding the process by which signals are transferred from the T cell receptor to the CD3 and CD4. This work explores the dynamic coordination of these coreceptor interactions during (dis)engagement of the membrane-bound CD4-CD3-TCR from the pMHC.

INTRODUCTION

Cellular sensation is defined, in part, by the (dis)engagement of membrane-bound protein-protein interactions that occur in dynamic disequilibrium. Understanding these molecular- and atomic-level interactions has required a modernization of tools to discern the in situ mechanics and kinetics that initiate transmembrane activation and propagation of downstream intracellular signaling. The suite of experimental tools at the frontier of signal trans-

duction (1–5) include the following: microphysiological systems (i.e., lab-on-a-chip) to examine cellular migration in physically tuned microenvironments (6–10), biomembrane force probes to control and quantify applied force on protein-protein interactions (11–15), and a host of multifaceted probing techniques that simultaneously capture in situ nonequilibrium protein kinetics and/or biochemical signaling in real time (e.g., micropipette aspiration (16–18), atomic force microscopy (19,20), optical tweezers (21,22), magnetic tweezers (18), laminar flow chamber (23–25)). However, none of these techniques provide atomic-level insight. More recently with the advent of enhanced computational speed and increasing availability of protein structures, long-timescale molecular dynamics simulations have been added to the suite of tools to

uniquely capture atomic-level insight on protein-protein association and dissociation (26–29).

A central feature of the adaptive immune response is the (dis)engagement of the peptide-major histocompatibility complex (pMHC) with the T cell receptor (TCR), which may (or may not) result in the activation of the T cell and effector function. Atomic-level understanding of this process is limited yet fundamental to advance TCR design as a central feature of immunotherapies. The TCR is stabilized, in part, by a three-dimer coreceptor ($\delta\varepsilon$ and $\gamma\varepsilon$ heterodimers and $\zeta\zeta$ homodimers) known as the CD3 (30–33) that is required for localization of the TCR to the cell surface (34). TCR cell signaling is initiated by binding to a cognate pMHC. It is not yet known which amino acids in the TCR dominate the interactions during (dis)engagement and whether engagement, disengagement, or both initiate signal transduction to the intracellular domain of the CD3 coreceptor where 10 immunoreceptor tyrosine-based activation motifs (ITAMs) are phosphorylated by lymphocyte-specific kinases (LCKs) (35).

In addition to the CD3 coreceptor, the TCR complex includes the CD4 or CD8 coreceptor, which has a dual role in localizing the LCKs to the cell membrane through the interaction of the cytoplasmic tail of the CD4 or CD8 coreceptor (36,37), as well as stabilizing the extracellular TCR-pMHC interaction (38,39). The transmembrane mechanism by which CD3 ITAM phosphorylation is enabled by the TCR (dis)engagement to a cognate pMHC remains debated (35,40). In brief, the cytoplasmic chains of the CD3 are thought to be sequestered to the lipid bilayer preventing ITAM phosphorylation until the (dis)engagement from a cognate pMHC releases the ITAMs from the inner membrane (35,40). The mechanism by which signal is transferred from the TCR-pMHC interaction to the CD3 ITAMs is unknown but may be mechanically transduced (2–5,41). Moreover, despite demonstration that the coordinated trimolecular (CD4-CD3-TCR or CD3-TCR-CD8) disengagement from the pMHC amplifies molecular bond lifetime under load and enhances antigen discrimination (42,43), there is no atomic-level understanding of how this trimolecular coordination is achieved.

We began this investigation by utilizing the recently deposited CD3-TCR complex (30) to construct two biomimetic models: a CD3-TCR-pMHC and a CD4-CD3-TCR-pMHC complex embedded in a lipid bilayer (44). This approach allows us to specifically probe the impact of the CD4 coreceptor on the TCR-pMHC (dis)engagement. We equilibrated these molecular systems at physiological conditions to simulate engagement and then used steered molecular dynamics to pull the pMHC from the TCR complexes to simulate disengagement. We then quantitatively analyzed the interaction energy and relative motion of the system subcomponents to provide atomic-level mechanistic insight on the impact of the CD4 coreceptor on the (dis)engagement process.

MATERIALS AND METHODS

Superposition and homology modeling

The cryo-EM structure of the CD3-TCR complex (30) (PDB: 3TOE) is the starting structure for generating the CD3-TCR-pMHC and CD4-CD3-TCR-pMHC systems. Next, the TCR from the deposited TCR-CD4-pMHC cocrystal structure (38) (PDB: 6JXR) is superimposed and fused on the TCR from the CD3-TCR complex using PyMOL (Schrodinger; New York, NY). The TCR is the MS2-3C8 that engages the self-peptide derived from myelin basic protein (MBP$_{114\text{-}126}$, FSWGAEGQRPGFG) in complex with HLA-DR4 at a measured K_D 5.0 μM in solution (45). Moreover, the CD4 was subjected to directed-evolution by random in vitro mutagenesis to increase affinity to HLA-DR4 (K_D = 10.1 μM) (38). This CD4 complex has enhanced affinity to the pMHC compared with the wild-type; however, the wild-type cocrystal structure is not available, and the TCR affinity is still stronger than the mutant CD4, so we determined this was sufficient for this initial investigation. Future work may elucidate the effects of additional CD4 mutants on TCR-CD3-CD4-pMHC (dis)engagement. Next, the CD4 intracellular domain (46) is attached to the N-terminus of the CD4 by generating a set of 10 structures with the lowest DOPE score (47) via Modeller v10.1 (48,49). The final CD4-CD3-TCR-pMHC system was selected by assessing the ability of the system to be embedded in a lipid bilayer (see below), largely determined by the relative orientation of the CD3 and CD4 transmembrane domains. The CD3-TCR-pMHC system was generated from the CD4-CD3-TCR-pMHC system by removing CD4 before the lipid bilayer embedding. We aimed primarily to understand the effects of pMHC (dis)engagement on the T cell (TCR, CD3, CD4, and membrane) and thus elected not to embed the pMHC in a membrane. This limitation may be the subject of future investigation; however, solution-based pMHCs have been shown to activate T cells in vitro (50,51). The CD3 ITAM motif structures and the relative membrane orientation are not known, so we decided it was premature to predict their structure from sequence via homology modeling or deep learning. This allowed us to primarily focus on the effect of the CD4 on pMHC dissociation; however, the CD3 ITAM modeling is an important and nontrivial future direction of research. Moreover, recently deposited CD3-TCR complexes (52,53) allow additional investigations of CD3-TCR-CD8 and CD4-CD3-TCR association and dissociation from the pMHC. In addition, these structures allow for future exploration of the inhibiting effects of cholesterol bound to the TCR transmembrane domain (53).

Lipid bilayer and protein embedding

The heterogeneous lipid bilayers were constructed using the CHARMM-GUI membrane builder (54). The CHARMM-GUI generates output files for GROMACS simulations in six steps (55–60): 1) protein coordinates are read from the CD3-TCR-pMHC and CD4-CD3-TCR-pMHC system; 2) proteins are then oriented by aligning the first principal axis along the z axis; 3) determination of system size by specifying lipid ratios and an initial guess (20 $\times$ 20 nm^2) for bilayer xy area; 4) components are built around the protein including the lipid bilayer, solvent, and ions; 5) components are assembled into GROMACS formatted topology; and 6) files are output for multistep energy minimization and equilibration.

The $\sim$20 $\times$ 20 nm^2 biomimetic bilayers consist of 1600 lipids (800 in the upper and 800 in the lower leaflet). The lipid bilayer is evenly divided across leaflets and in total consists of 784/1600 cholesterol (CHL1), 304/1600 phosphatidylcholine (POPC), 272/1600 phosphatidylserine (SOPS), 128/1600 ceramide (CER160), 96/1600 dioleoylphosphatidylethanolamine (DOPE), and 16/1600 phosphatidylinositol (SAPI). Importantly, lipid order and molar ratios have been shown to affect T cell function (61). Therefore, the lipid molar ratios were determined from measured mass spectrometric lipid analysis in activated Jurkat T cells (44). Activated T cells contained $\sim$49% cholesterol, $\sim$19% PC, $\sim$17% PS, $\sim$8% SM, $\sim$6% PE, and $\sim$1% PI. In this work, we

TABLE 1 System atom restraints for six-step relaxation

Relaxation step	Ensemble	Time step	Relaxation time	Force constants for restraints					
				Protein back bone[a]	Protein side chain[a]	Lipid head[b]	Lipid tail[c]	Water[b]	Ions[a]
1	NVT	1 fs	125 ps	40	20	10	10	2.5	10
2	NVT	1 fs	125 ps	20	10	4	4	2.5	0
3	NPT	1 fs	125 ps	10	5	4	2	1.0	0
4	NPT	2 fs	500 ps	5	2	2	2	0.5	0
5	NPT	2 fs	500 ps	2	0.5	0.4	1	0.1	0
6	NPT	2 fs	500 ps	0.5	0	0	0	0	0

[a]Positional harmonic restraints (x, y, z) in kcal/mol$\cdot$Å^2
[b]Positional harmonic restraints (z) in kcal/mol$\cdot$Å^2
[c]Dihedral restraints in kJ/mol$\cdot$rad^2

used the ceramide, CER160, as surrogate for the sphingomyelin (SM) moiety, which is a class of sphingolipids containing a sphingosine core, neutrally charged headgroup, and representative lipid tails (18:1/16:0). Moreover, although the basal ceramide levels were not detected in the mass spectrometry analysis, sphingomyelinase, which hydrolyzes sphingomyelin to ceramide, has been shown to be upregulated in stimulated T cells essential for signal amplification (62,63), and ceramide colocalizes with TCR-CD3 in activated T cells (64).Therefore, due to the spatiotemporal limitations of mass spectrometry and the importance of localized ceramide in activated T cells, we elected to replace sphingomyelin with the hydrolyzed version, ceramide CER160. The membrane potential of activated T cells is ~50 mV (65,66), and the lipid charge density is ~0.00055 protons/nm^2 for this 400-nm^2 lipid bilayer $(\rho = \frac{\Delta V \varepsilon_0}{x})$. Therefore, the net charge across the upper and lower leaflet is neutral. Extended preproduction molecular dynamics simulations are performed to model the protein-lipid systems at physiological conditions (details below) and minimize artifacts from superposition, homology modeling, and lipid bilayer embedding.

Molecular dynamics setup

The output files from CHARMM-GUI were the starting point for the subsequent molecular simulations. In CHARMM-GUI (54), titratable protein residues were determined by calculation of pKa and deprotonated if pKa was below 7.4. Systems were solvated in rectangular water boxes with the TIP3P water model large enough to satisfy minimum image convention. Na$^+$ and Cl$^-$ were added to neutralize the protein charge and to reach physiologic salt concentration of ~150 mM. Simulations were performed in full atomistic detail using the CHARMM36 all-atom lipid force field (67,68) with orthorhombic periodic boundary conditions. The protein groups were indexed by atom count in the structure files: MHC (atoms = 1–2873, 3084–5976), peptide (atoms = 2874–3083), CD3 (atoms = 5977–14508), TCR (atoms = 14,509–22794), and CD4 (atoms = 22,795–29723). Lipids are included in the topology file and indexed according to atoms in their headgroup and stereospecific numbered tails (sn1 & sn2): CHL1 (headgroup = O3 | sn1 = n/a | sn2 = n/a), POPC (headgroup = P,N,C11 | sn1 = C31–316 | sn2 = C21–C218), SOPS (headgroup = P,N,O13A | sn1 = C31–C318 | sn2 = C21–C218), CER160 (headgroup = NF,O1,C1S | sn1 = C2S–C18S | sn2 = C1F–C16F), DOPE (headgroup = P, N,C11 | sn1 = C31–C318 | sn2 = C21–C218), and SAPI (headgroup = P,C11,C14 | sn1 = C31–C318 | sn2 = C21–C220).

TABLE 2 TCR-pMHC system preproduction simulation constituents

TCR-pMHC system	Water Molecules	Ions	Total Atoms
CD3-TCR-pMHC	256,064	1015 Na$^+$, 710 Cl$^-$	928,634
CD4-CD3-TCR-pMHC	247,032	1017 Na$^+$, 689 Cl$^-$	962,680

Energy minimization, equilibration, and preproduction

The assembled systems undergo several relaxation steps (with restraints) before the unrestrained molecular dynamics preproduction simulations. All steps are performed in GROMACS 2021.3 (69,70) with domain decomposition on 4 AMD EPYC 7532 32-Core Processors. First is steepest descent energy minimization to ensure correct geometry and absence of steric clashes. Next, a six-step relaxation (Table 1) with various restraints that are progressively relaxed on the protein, water, ions, and lipids is provided by CHARMM-GUI (55–60): 1) harmonic restraints on ions and protein heavy atoms, 2) planar restraints on water to prevent diffusion into the membrane's hydrophobic region, and 3) planar restraints on the lipid headgroups to prevent migration along the z axis. The restraint forces are progressively relaxed to avoid dynamic integration instability while relaxing the systems to temperature (310 K) and pressure (1.0 bar). The first two relaxation steps are in the constant volume ensemble (NVT), and the remaining four steps are in the constant pressure ensemble (NPT).

Preproduction MD runs used the Nose-Hoover thermostat (71) and Parrinello-Rahman barostat (72) to ensure true ensemble sampling and to maintain temperature and pressure, respectively. Temperature was maintained by coupling all protein, lipid, and solvent atoms to separate baths. Pressure and temperature time constants 5.0 and 1.0 ps, respectively, were used with the isothermal compressibility of water, 4.5 x 10^{-5} bar^{-1}. Box sizes after preproduction runs were 18.68105 × 18.68105 × 26.02621 nm^3 (CD3-TCR-pMHC) and 18.6705 × 18.6705 × 27.04916 nm^3 (CD4-CD3-TCR-pMHC) with ~250,000 water molecules, ~1700 ions, and ~900,000 total atoms (Table 2). The particle Ewald mesh algorithm (73,74) was used for long-range electrostatic calculations with cubic interpolation and 0.12-nm maximum grid spacing. Short-range nonbonded interactions were cut off at 1.2 nm. All bond lengths were constrained using the LINCS algorithm (75); except, water bond lengths were constrained by SETTLE (76). The leap-frog algorithm was used for integrating equations of motion with 2-fs time steps. Two metrics were used to assess the convergence of the preproduction simulations for steered molecular dynamics: 1) the root mean-square deviation (RMSD) from the initial configuration of all protein groups (TCR, CD3, CD4, peptide, MHC) and 2) average area per lipid for the upper and lower leaflets. The converged preproduction simulations were considered complete once both metrics had flattened for at least 50 ns of simulation time. This resulted in 150-ns and 300-ns preproduction runs for the CD3-TCR-pMHC and CD4-CD3-TCR-pMHC systems, respectively. Three configurations were selected from the CD3-TCR-pMHC system (100, 125, 150 ns) and the CD4-CD3-TCR-pMHC system (250, 275, 300 ns) preproduction runs to minimize time-correlated structures (77) and enhance steered molecular dynamics (SMD) sampling (78).

Steered molecular dynamics

After the preproduction runs, the protein-lipid configurations were selected 25 ns apart in the 50-ns time windows and solvated in simulation boxes with an extended z axis: 18.68105 × 18.68105 × 44.02621 nm^3

TABLE 3 TCR-pMHC system steered molecular dynamics simulation constituents

TCR-pMHC system	Preproduction equilibration time (ns)	Water Molecules	Ions	Total Atoms
CD3-TCR-pMHC	100	442,854	1714 Na$^+$, 1388 Cl$^-$	1,517,498
	125	442,913	1714 Na$^+$, 1388 Cl$^-$	1,517,675
	150	442,888	1714 Na$^+$, 1388 Cl$^-$	1,517,600
CD4-CD3-TCR-pMHC	250	452,280	1724 Na$^+$, 1419 Cl$^-$	1,552,746
	275	452,280	1724 Na$^+$, 1419 Cl$^-$	1,552,746
	300	452,280	1724 Na$^+$, 1419 Cl$^-$	1,552,746

(CD3-TCR-pMHC) and $18.6705 \times 18.6705 \times 45.04916$ nm^3 (CD4-CD3-TCR-pMHC). SMD system details are provided (Table 3), and the 18-nm box extension was sufficient to separate the pMHC and was based on our previous work (29,79–81). Solvation was followed by 1) the addition of Na$^+$ and Cl$^-$ ions, 2) 100 ps NVT, and 3) 100 ps NPT as described previously to relax re-solvated water-ion boxes (with no restraints) (29,79–81). There are two ways to apply load (82): controlling pull force (29,59,60,84) or pull rate (17,18). Both methods are readily used in the literature, and we selected to control pulling force to focus, in part, on comparing the force-dependent dissociation kinetics of the TCR-pMHC systems. As an improvement on our previous reports (29,59,60) and previous studies (17,18), we chose to apply a constant force of 250 pN to the center of mass (COM) of the lipid membrane and pMHC in the z-direction, until the distance between the COMs reached 0.49 times the box size. This was more than adequate to fully separate the CD3-TCR and CD4-CD3-TCR systems apart from the pMHC (i.e., interaction energy with pMHC reached zero). The break point is defined as the point where the interaction energy (both Coulombic and Lennard-Jones) reaches zero between the TCR-pMHC, which corresponded to $\xi = 16.3$ nm $\pm$ 0.66 across the six steered MD runs. The COM of the membrane was chosen as the pulling location to mimic the in situ TCR, and pulling from the COM of pMHC was selected because pulling from the termini results in artificial unfolding (29). Although force is critical in TCR-pMHC interactions (14,83), it remains difficult to interpret and measure the direction of applied force on the nanometer scale (84). A previous investigation exploring force directions found minimal binding dependence on force direction across TCR-pMHC pairs (17), and thus we elected to pull perpendicular to the lipid membrane to ensure full separation from the membrane-coreceptor complex. All simulation trajectories and selected frames were visualized in the PyMOL Molecular Graphics System (Schrodinger; New York, NY).

Data and statistical analysis

Data analysis was performed with the GROMACS suite (69,70) (i.e., gmx make_ndx, gmx hbond, gmx rms, gmx_rdf, gmx_density, gmx rmsf, and gmx_energy) and python packages for data handling and visualization (i.e., numpy (85), pandas (86), matplotlib (87), GromacsWrapper (88), scipy (89), and pingouin (90), and custom python scripts). The geometry of a Lennard-Jones contact is defined as a distance less than 0.35 nm between atoms. The principal component analysis of the simulation trajectories was performed using the package MD analysis (91,92). FATSLiM (93) was used for calculating area per lipid, and LiPyphilic (94) was used for calculating area per lipid, lipid order parameter, assigning lipid leaflets, and 2D Voronoi tessellations. Statistics were performed in python using scipy for Student's t-tests, scipy for one-way analysis of variance (ANOVA), and pingouin for pairwise Tukey-HSD post-hoc tests.

RESULTS

The solved CD3-TCR complex (30) was superimposed on the TCR of the TCR-pMHC-CD4 complex (38). The CD4 was then homology modeled (47–49) to include the cytoplasmic tail (46). Next, the CD3-TCR-pMHC and CD4-CD3-TCR-pMHC complexes (Fig. 1) were embedded in a lipid bilayer composed of lipids at the stoichiometric ratio to model activated T cells (44). The systems were solvated, multistep energy minimized, and simulated with no restraints for 150 ns without CD4 and 300 ns with CD4 to equilibrate the protein-lipid structures at physiological conditions (see Materials and Methods). Consistent with previous work, during the unrestrained molecular dynamics simulations, all protein chains and lipids were monitored, and the equilibration point was indicated by flattening of the RMSD (Fig. S1 A and B) and area per lipid (Fig. S1 C and D) plots, respectively (95–97). The CD3-TCR-pMHC and CD4-CD3-TCR-pMHC systems reached equilibrium after ~100 ns and ~250 ns of simulation time, respectively.

The lipid distributions were analyzed in the upper and lower leaflet of both CD3-TCR-pMHC (Fig. 2 A) and CD4-CD3-TCR-pMHC (Fig. 2 B) systems after equilibration. We found that the lipids were uniformly distributed around the proteins with an area per lipid between 0.4 and 1.0 nm^2 in the upper and lower leaflet (Fig. 2 C and D). Moreover, heterogeneous membrane normal lipid densities were between 50 and 600 kg/m^3 (Fig. 2 E and F). In addition, we assessed the individual lipids by analyzing the area per lipid and lipid order parameter in the upper and lower leaflet (Figs. S2–S7). The area per lipid is the density of lipid headgroups in the leaflet plane, and the lipid order parameter is the averaged second Legendre polynomial of orientation of lipid tail heavy atoms with respect to the membrane normal. We found that CHL1 is uniformly distributed in the bilayer, and the area per lipid is ~1–2 nm^2, which is consistent with the molar ratio (Fig. S2). Similarly, POPC (Fig. S3), SOPS (Fig. S4), ceramide (CER160) (Fig. S5), DOPE (Fig. S6), and SAPI (Fig. S7) lipids are evenly distributed with an area per lipid proportional to their molar ratio. Moreover, the average order parameter of lipid tails is between 0.2 and 0.5 for POPC, SOPS, CER160, DOPE, and SAPI (Figs. S3–S7).

To effectively capture the ensemble of possible configurations at equilibrium, we selected configurations in triplicate after the equilibration point and used SMD to pull apart (dissociate or disengage) the CD3-TCR-pMHC and CD4-CD3-TCR-pMHC complexes from each configuration (Fig. 3 A–C). In total, each system is approximately ~1.5 million atoms with a summation of ~1 μs of simulation time (Table 3). We found that, under load, the presence of CD4 significantly increases the average TCR-pMHC bond
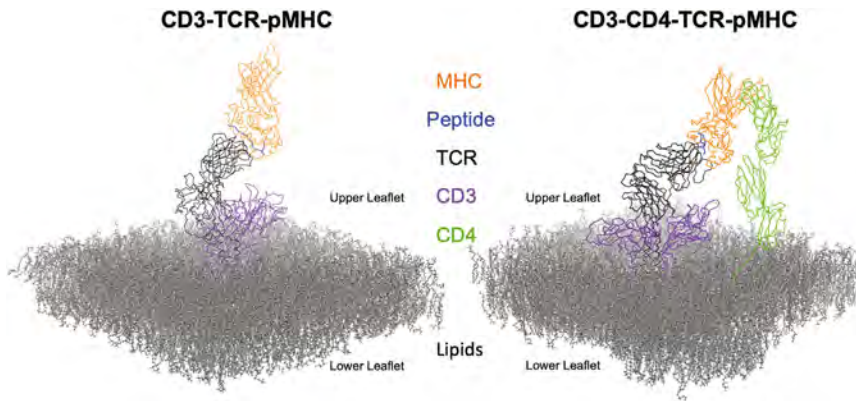
FIGURE 1 TCR-pMHC systems. Protein-membrane systems include (*left*) the CD3-TCR-pMHC and (*right*) the CD4-CD3-TCR-pMHC protein complex embedded in a lipid bilayer. System groups are color coded: TCR (*black*), CD3 (*purple*), CD4 (*green*), peptide (*blue*), MHC (orange), and lipids (*gray*). To see this figure in color, go online.

lifetime from 6.4 ns to 282.7 ns (Fig. 3 *A*). At equilibrium, the pMHC is confined 1.80 nm closer ($\xi_0 = 11.5 \pm 0.28$ nm compared with $\xi_0 = 13.3 \pm 0.32$ nm) to the T cell membrane in the presence of the CD4 coreceptor (Fig. 3 *D* and

E). Furthermore, this CD4 confinement substantially increases the coulombic interaction energy (about eightfold) between the TCR-pMHC at the initial reaction coordinate, ξ_0, and is maintained (about twofold) along the reaction
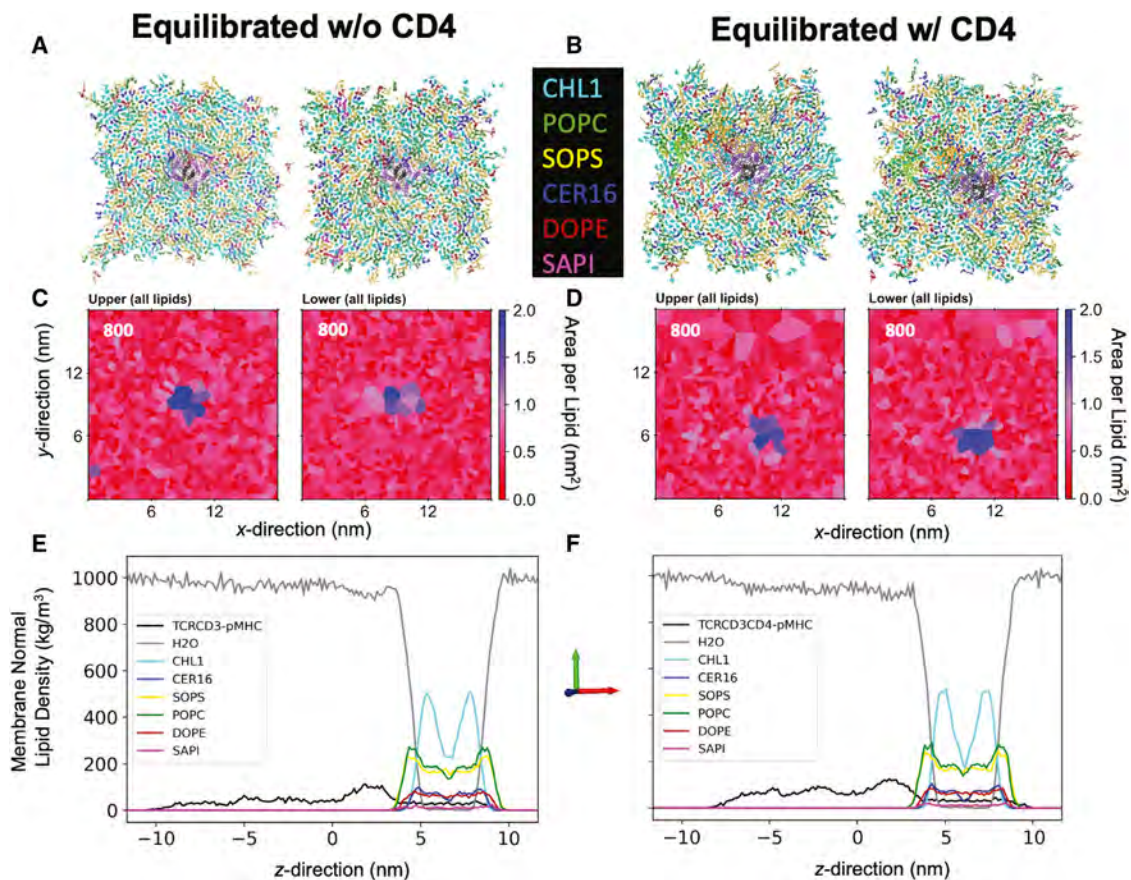

FIGURE 2 TCR-pMHC system lipid profiles. The lipid profiles for the CD3-TCR-pMHC (*left*) and CD4-CD3-TCR-pMHC (*right*) systems. This includes views of the lipid membrane: top-down view of the upper leaflet for system without CD4 (*A, left*) and system with CD4 (*B, left*) as well as bottom-up view of the lower leaflet for system without CD4 (*A, right*) and system with CD4 (*B, right*). The lipid color schematic: CHL1 (*cyan*), POPC (*forest green*), SOPS (*yellow*), CER160 (*blue*), DOPE (*brick red*), SAPI (*magenta*). Protein components are also depicted in the top row in the same color schematic as Figure 1. 2D Voronoi tessellations (*x-y plane*) of the lipid headgroups' area per lipid for the system without CD4 (*C*) and with CD4 (*D*) for the upper (*left*) and lower (*right*) leaflet. Lipid count for the upper and lower leaflet is provided in the top left of each area per lipid plot. Membrane normal (*z axis*) densities of all system components for CD3-TCR-pMHC system (*E*) and CD4-CD3-TCR-pMHC (*F*). The unit vectors are displayed in a cartesian coordinate system. To see this figure in color, go online.
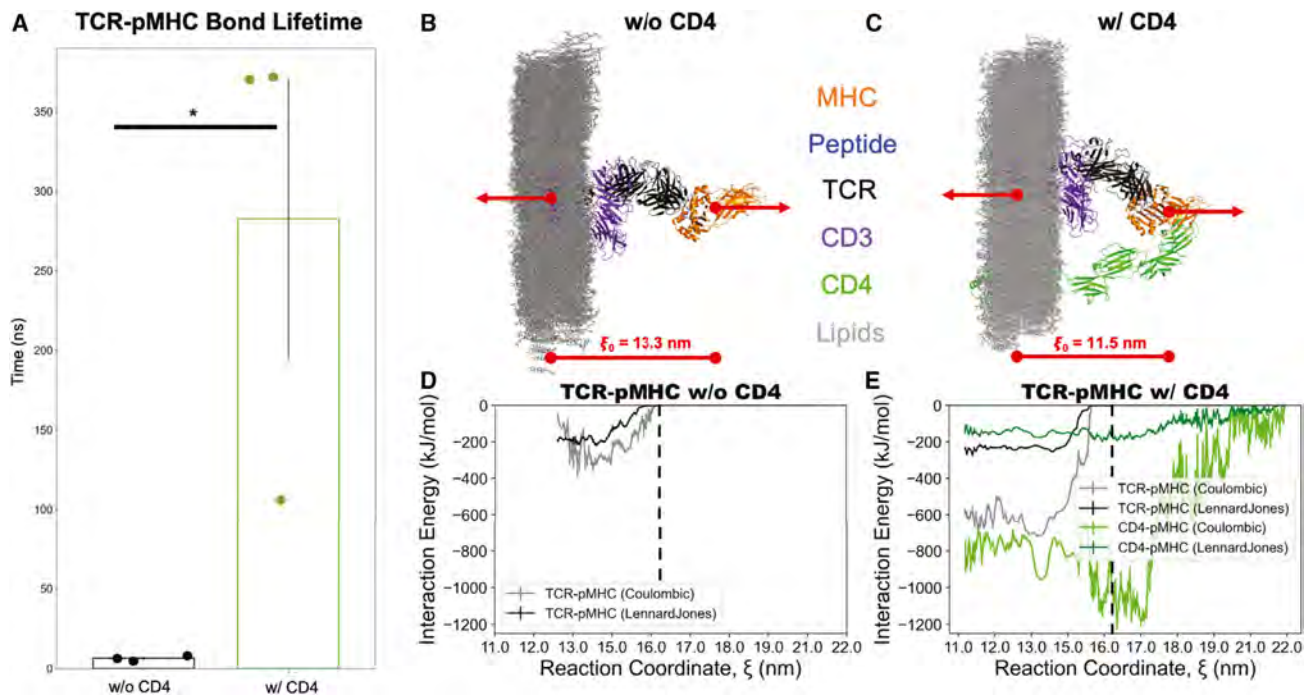
FIGURE 3 TCR-pMHC dissociation. The kinetics and energetics of pMHC dissociation. (*A*) Average TCR-pMHC bond lifetime in nanoseconds for the system without CD4 (*left*) and with CD4 (*right*). Systems are statistically compared (n = 3): #$p < 0.10$, *$p < 0.05$, **$p < 0.01$, ***$p < 0.001$ by one-way ANOVA followed by Tukey-HSD post-hoc test. Graphical representation of steered molecular dynamics for system (*B*) without CD4 and (*C*) with CD4. System groups are color coded: TCR (*black*), CD3 (*purple*), CD4 (*green*), peptide (*blue*), MHC (*orange*), and lipids (*gray*). The red arrows indicate the site and direction of applied force. The bottom red lines with red circles at both terminals indicate the initial reaction coordinate, ξ_0, for each system in nanometers. Interaction energy as a function of the reaction coordinate is displayed for (*D*) the CD3-TCR-pMHC system and (*E*) the CD4-CD3-TCR-pMHC system. Interaction energy between the TCR and pMHC is decoupled into coulombic (*gray*) and Lennard-Jones (*black*) potential. Additionally, for the CD4-CD3-TCR-pMHC system, the CD4-pMHC coulombic (*green*) and Lennard-Jones (*forest green*) potential is shown. The interaction energies are recorded at 10-ps intervals and distributed into ~0.5-Å bins where the lines represent mean ± SEM across triplicate steered MD runs. The TCR-pMHC break point, $\xi_{=16.3}$ nm, is indicated by the dashed vertical line. To see this figure in color, go online.

coordinate (Fig. 3 *D* and *E*). Moreover, the coulombic interaction energy between the CD4-pMHC is ~ –100 to –200 kJ/mol greater than the TCR-pMHC. This coordinated CD4 binding to the pMHC is further strengthened by ~ –400 kJ/mol at $\xi = 16.3$ nm, which corresponds to the average break point of the TCR-pMHC interaction (Fig. 3 *E*). The pMHC breakpoint when CD4 was present was 15.9 ± 0.6 nm, and the break point when CD4 was not present was 16.6 ± 0.6 nm. This closer break point in the presence of CD4 is likely because the pMHC configuration is 1.8 nm closer to the membrane at equilibrium. Interestingly, this results in a longer reaction distance of 4.4 nm in the presence of the CD4 (i.e., 15.9 nm–11.5 nm) compared with 3.3 nm in the absence of CD4 (i.e., 16.6 nm–13.3 nm).

Next, we analyzed the hydrogen bonds and Lennard-Jones contacts between the TCR-pMHC to discern the characteristic residues that contribute to the spatial and dynamic energetics. During the pulling simulations of the CD3-TCR-pMHC and CD4-CD3-TCR-pMHC systems, we found significantly more hydrogen bonds between the TCR-pMHC in the presence of the CD4 coreceptor during dissociation (Fig. 4 *A*). In summation with the CD4-pMHC interactions, the CD4-CD3-TCR complex has on average

17.4 hydrogen bonds with the pMHC (TCR-pMHC (8.8 ± 2.4) + CD4-pMHC (8.6 ± 3.0)) compared with only 3.8 ± 1.9 hydrogen bonds for the CD3-TCR complex (Fig. 4 *A*). To understand the differences in the TCR-pMHC interactions, we evaluated the total percentage of simulation time that all hydrogen bonds were occupied for each system. We then examined the top five hydrogen bonds ranked by occupancy percentage for each system (Fig. 4 *B*). Interestingly, we found asymmetric hydrogen bonding during dissociation. For example, the TCR arginine 115 demonstrated 97.8% occupancy to the peptide arginine 9 for the CD4-CD3-TCR-pMHC system compared with 0.0% occupancy for the CD3-TCR-pMHC system. Conversely, the TCR glycine 115 demonstrated a 28.0% occupancy hydrogen bond to the peptide alanine 5 for the CD3-TCR-pMHC system compared with 0.0% occupancy for the CD4-CD3-TCR-pMHC system. These asymmetric interactions are highlighted by the shift in interaction "hotspots" at the TCR-pMHC interface (Fig. S8). This shift is initiated during the preproduction equilibration of the systems, and the asymmetry in bonding is measured during the SMD dissociations. Similarly, the number of Lennard-Jones contacts between the
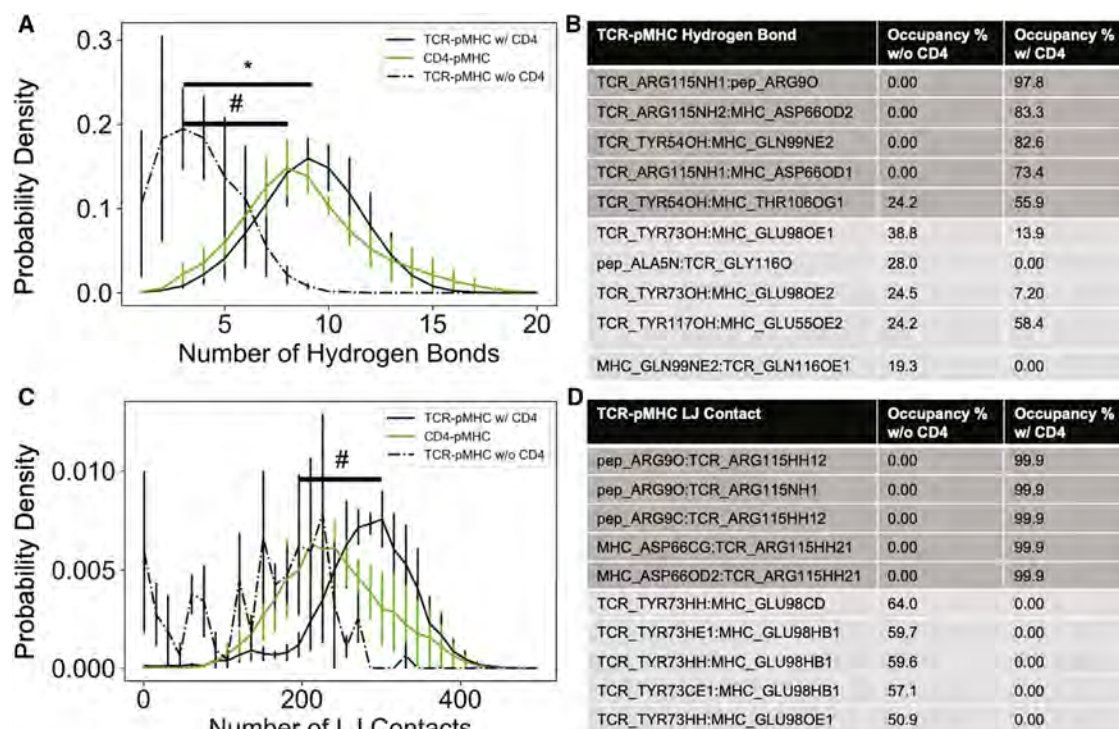
FIGURE 4 TCR-pMHC bonds. Hydrogen bonds and Lennard-Jones contacts for the CD3-TCR-pMHC and CD4-CD3-TCR-pMHC systems. This includes (*A*) the probability density of hydrogen bonds between the TCR-pMHC and CD4-pMHC for each system, (*B*) the top five hydrogen bonds between TCR-pMHC for each system (10 total), (*C*) the probability density of Lennard-Jones contacts between the TCR-pMHC and CD4-pMHC for each system, (*D*) and the top five Lennard-Jones contacts between TCR-pMHC for each system (10 total) (*right*). The top five interactions for the CD3-TCR-pMHC system are colored light gray, and the top five interactions for the CD4-CD3-TCR-pMHC system are colored dark gray. Systems are statistically compared (n = 3): #$p <$ 0.10, *$p <$ 0.05, **$p <$ 0.01, ***$p <$ 0.001 by one-way ANOVA followed by Tukey-HSD post-hoc test. To see this figure in color, go online.

TCR-pMHC was significantly greater for the CD4-CD3-TCR-pMHC system (Fig. 4 *C*), and there were comparable asymmetric interactions between the systems (Fig. 4 *D*). Furthermore, we generated heat maps for the hydrogen bonds and Lennard-Jones contacts as a function of the reaction coordinate by distributing the time points into ~0.5-Å bins and calculating the fractional occupancy of each respective bin. These heat maps were averaged over the triplicate pulling simulations for each system, and the top ten interactions are displayed for each system for comparison (Fig. S9). The heat maps again demonstrate a significant shift in the amino acids contributing to the hydrogen bonds and Lennard-Jones contacts.

To postulate a potential mechanism for how disengagement of the TCR-pMHC may generate a mechanical perturbation, and thus a signal, that is transferred to the CD3, we examined the CD3-TCR, CD3-lipids, and lipid-lipid interactions during (dis)engagement. We found that the CD3-TCR interaction energy along the reaction coordinate is similar in magnitude for both the CD3-TCR-pMHC and CD4-CD3-TCR-pMHC systems (Fig. 5 *A*); however, there are increased energetic fluctuations ($\pm$ 200 kJ/mol) near and after the TCR-pMHC break point, ξ = 16.3 nm (Fig. 5 *A*). Moreover, these energetic fluctuations persist near and through this reaction coordinate for the CD3-lipids

(Fig. 5 *B*) and lipid-lipid interactions (Fig. 5 *C* and *D*). With a fixed reaction coordinate (i.e., near the TCR-pMHC break point), the overlayed structures at the peak and trough of energetic fluctuation demonstrate structural oscillation in the CD3-TCR complex for both systems (Fig. S10). For example, the CD3-TCR without CD4 fluctuates coulombic potential between −1871 kJ/mol and −1603 kJ/mol with a CD3-TCR RMSD of 1.49 nm after membrane alignment (Fig. S10 *A*). Additionally, the CD3-TCR with CD4 fluctuates coulombic potential between −2016 kJ/mol and −2447 kJ/mol with a CD3-TCR RMSD of 2.36 nm after membrane alignment (Fig. S10 *B*). These structural oscillations are supported by the principal component analysis of the trajectories (Videos S1–S12). For the CD3-TCR-pMHC system, the first principal component (PC1) is dominated by the direction of pulling, and PC2–5 are dominated by various scissor and twist motions of the CD3-TCR (Fig. S11; Videos S1–S12). For the CD4-CD3-TCR-pMHC system, PC1 is dominated by the CD4 translocation to stabilize the CD3-TCR-pMHC, PC2 is dominated by the direction of pulling, and PC3–5 are dominated by CD3-TCR scissor and twist motions (Fig. S11; Videos S1–S12). Importantly, the CD4 translocation, demonstrated by PC1, is further supported by an increase in coulombic energy between CD4-pMHC (Fig. 3 *E*) near the TCR-pMHC break
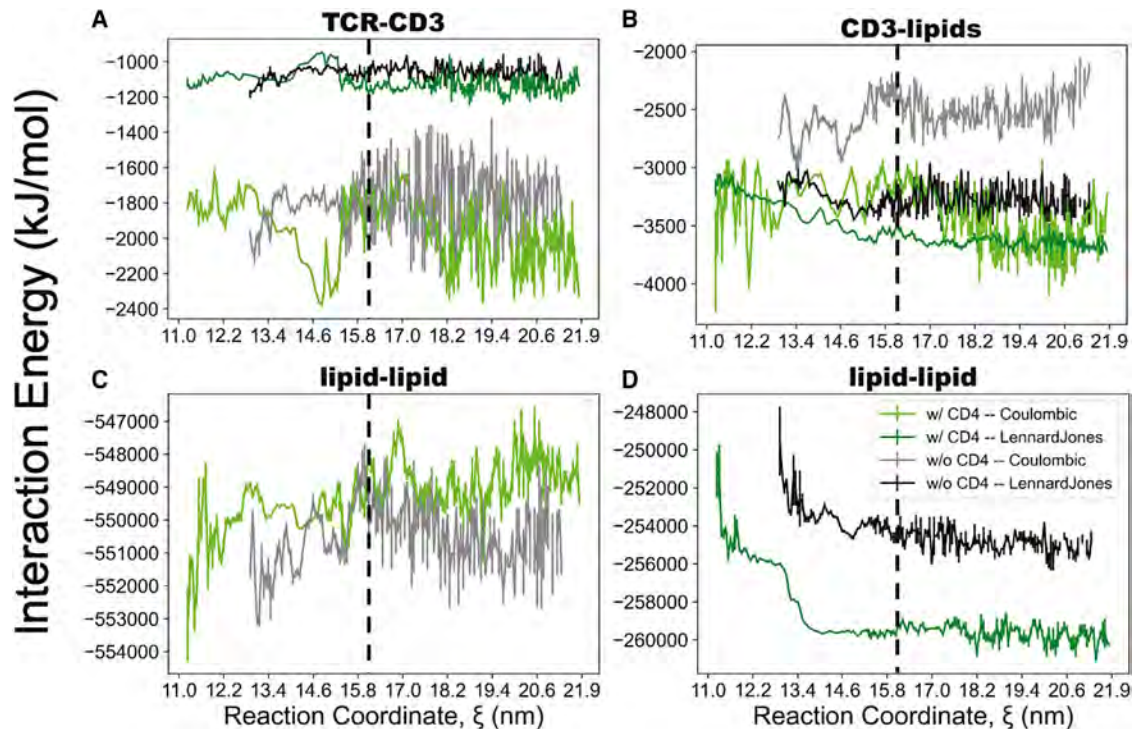
FIGURE 5   CD3-TCR, CD3-lipids, and lipid-lipid interactions. Interaction energy as a function of the reaction coordinate is displayed for the CD3-TCR-pMHC and CD4-CD3-TCR-pMHC systems. Interaction energy is decoupled into coulombic (*gray*, *green*) and Lennard-Jones (*black*, *forest green*) potential for the respective systems (CD3-TCR-pMHC, CD4-CD3-TCR-pMHC). This includes the (*A*) CD3-TCR, (*B*) CD3-lipids, (*C*) lipid-lipid coulombic potential, and (*D*) lipid-lipid Lennard-Jones potential. The interaction energies are recorded at 10-ps intervals and distributed into ∼0.5-Å bins where the lines represent mean ± SEM across triplicate steered MD runs. The TCR-pMHC break point, $\xi_{=16.3}$ nm, is indicated by the dashed vertical line. To see this figure in color, go online.

point. Moreover, this translocation results in additional stabilizing coulombic interactions between the CD4-TCR and CD4-CD3 (Figs. 6 and S12) that hinder dissociation.

DISCUSSION

The CD4 colocalizes with the CD3-TCR complex and hinders the dissociation of the TCR-pMHC. This trimolecular coordination is achieved by the CD4 1) confining the pMHC 1.80 nm closer to the T cell membrane, 2) increasing the strength of the TCR-pMHC interaction by shifting the TCR along the pMHC binding groove to engage a different complement of amino acids and about an additional five hydrogen bonds, and 3) translocating in proximity to the CD3-TCR-pMHC, effectively stabilizing the pMHC bound complex and hindering dissociation by 276.3 ns. Moreover, dissociation of the pMHC from the CD3-TCR and CD4-CD3-TCR complexes creates increased energetic and structural fluctuations that may contribute to signal transduction.

System equilibration

The TCR, CD3, pMHC, and lipid bilayer equilibrate with CD4 on timescales of tens of nanoseconds, thus requiring more simulation time than in the absence of CD4 (Fig. 1). The original cocrystal structure does not contain the membrane or the CD3 embedded TCR; therefore this reorientation is expected to accommodate the physiological state. Furthermore, to ensure an equilibrated state, we elongated the equilibration simulations to achieve at least a 50-ns window of stabilized structures (protein chains and lipids) to sample the triplicate configurations for SMD (Fig. S1).

The overall area per lipid of 0.4–1.0 nm^2 in the leaflets of the equilibrated systems (Fig. 2 *C* and *D*) is consistent with rigid lipid bilayers (98–101) such as the activated immunological synapse of a T cell (44,102). This rigidity can be attributed to a high lipid molar ratio 0.49 (784/1600) of CHL1 and the reduced lipid fluidity caused by hydrogen bonding from the cholesterol hydroxyl group to other lipid amide headgroups (103,104). Moreover, heterogeneous membrane normal lipid densities between 50 and 600 kg/m^3 (Fig. 2 *E* and *F*) reveal stable protein-lipid systems. We did not find any significant lipid-specific lateral diffusion around the membrane proteins during equilibration (not shown) or during the pulling simulation (Fig. S13). Moreover, lipids are evenly distributed around the membrane proteins (Figs. S2–S7). This may be attributed to reduced lateral lipid diffusivity in rigid (or CHL1-rich) membranes (104).
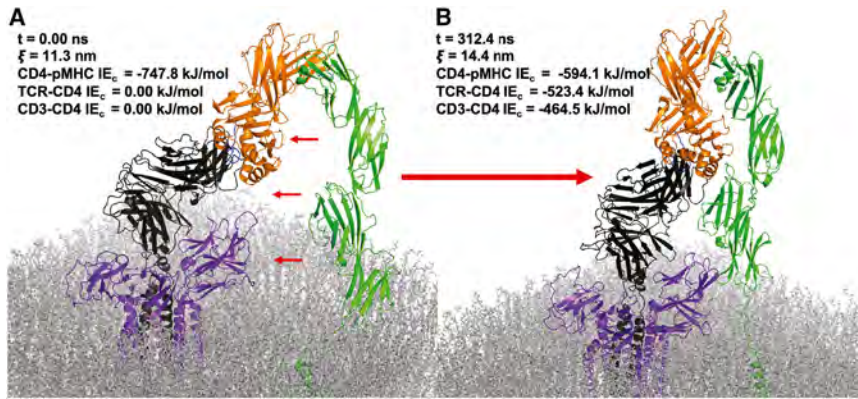
FIGURE 6 CD4 translocation. Visualization of the CD4 translocation to stabilize the TCR-pMHC interaction. This includes (*A*) the equilibrium configuration, which is also the starting point of the pMHC dissociation, and (*B*) a time point ~40 ns before the pMHC dissociates from the CD4-CD3-TCR complex. The configurational time point, reaction coordinate, CD4-pMHC coulombic potential, TCR-CD4 coulombic potential, and CD3-CD4 coulombic potential are displayed in the top left of each panel. Small red arrows indicate the direction of CD4 translocation. To see this figure in color, go online.

CD4 confinement, hindered dissociation, and translocation

We have previously demonstrated that SMD is robust at detecting small differences in protein-protein interactions including mutations and glycosylation (29,80). Moreover, mutations made to the peptide of the TCR-pMHC complex can alter the observed bond lifetime (79). However, prior work has not considered the CD3 and CD4 co-receptors and key contributors to the overall energetic landscape and thus possible contributors to the (dis)engagement of the pMHC-TCR. In this study, we demonstrate that the CD4 hinders TCR-pMHC dissociation by significantly increasing bond lifetime under load (Fig. 3 *A*), which is consistent with experimental bond lifetime measurements (42,43). This trimolecular coordination to increase bond lifetime has been shown to enhance antigen discrimination for CD4/CD8 T cells (42,43) and is consistent with a force-dependent kinetic proofreading model (29). Furthermore, we found that this bond lifetime augmentation is caused by three predominate structural changes. First, the CD4 confines the pMHC closer to the T cell membrane, $\xi_0 = 11.5$ nm with CD4 compared with $\xi_0 = 13.3$ nm without CD4 (Fig. 3 *B* and *C*).

Second, the CD4 confinement induces a TCR shift along the pMHC binding groove resulting in a stronger interaction (Fig. 3 *D* and *E*) and asymmetric bonding characteristics during dissociation (Fig. 4). For example, the coulombic interaction energy between the TCR-pMHC is about eight times stronger for the system with CD4 at ξ_0 and remains 200–300 kJ/mol stronger along the reaction coordinate (Fig. 3 *D* and *E*). The binding modes are formed after pre-production equilibration (ξ_0), and the measured binding asymmetry occurs during the SMD dissociations. These distinct binding characteristics are more easily visualized with hotspot residue interactions (Fig. S8) and made clear when the interaction heat maps are compared along the reaction coordinate during disengagement (Fig. S9). These observations are particularly intriguing as they identify an entirely different set of amino acids that dominate the inter-action energy landscape of the TCR-pMHC during (dis)engagement and thus provide new targets in the design of TCRs for immunotherapy.

Third, the CD4 translocation hinders pMHC dissociation by stabilizing the TCR-pMHC interaction. Stabilization is demonstrated by an increased coulombic potential of approximately –400 kJ/mol between the CD4-pMHC along the reaction coordinate beyond the TCR-pMHC break point, $\xi = 16.3$ nm (Fig. 3 *E*), resulting in a 44-fold increase in simulated bond lifetime (Fig. 3 *A*). Moreover, the CD4 translocation dominates essential atomic motion (i.e., PC1) (Fig. S11; Videos S1–S12) and results in additional stabilizing interactions of more than –500 kJ/mol between the TCR-CD4 and CD3-CD4 (Figs. 6 and S12). These findings agree with experimental measurements and provide an explanation for how trimolecular CD4-CD3-TCR complexes coordinate to enhance pMHC bond lifetime under load.

CD3-TCR oscillation

The release of sequestered CD3 ITAMs from the inner leaflet of the cell membrane is fundamental to T cell activation because TCRs do not have an intracellular signaling domain. The ability to understand transmembrane mechanotransduction from the TCR to CD3 is experimentally limited (105,106), and thus molecular dynamics provide an opportunity to explore interprotein conformational mechanisms across the lipid bilayer (107–109). In this study, we demonstrate that upon dissociation of a CD3-TCR or CD4-CD3-TCR complex from a cognate pMHC, there are increased energetic and structural fluctuations that occur between the CD3-TCR, CD3-lipids, and lipid-lipid. Superimposed structures at the peak and trough of energetic fluctuation demonstrate structural oscillation in the CD3-TCR complex with an RMSD of 1.49 nm for the system without CD4 and RMSD of 2.36 nm with CD4 (Fig. S10). These structural oscillations between the CD3-TCR exhibit corresponding energetic fluctuations upward of ± 134 kJ/mol without CD4

(Fig. S10 A) and ± 215.5 kJ/mol with CD4 (Fig. S10 B) near and beyond the TCR-pMHC break point, $\xi = 16.3$ nm (Fig. 5 A). These energetic fluctuations are propagated to the CD3-lipid (Fig. 5 B) and lipid-lipid (Fig. 5 C and D) interactions upon dissociation of the pMHC. Moreover, these structural fluctuations dominate the essential atomic motion and present as various scissor and twist motions of the CD3-TCR complex: PC2–5 without CD4 and PC3–5 with CD4 (Fig. S11; Videos S1–S12). These results suggest that the TCR rocks or wobbles upon disengagement of a cognate pMHC, and this motion propagates energy to the CD3-TCR and CD3-lipid interactions. The energetic fluctuations may contribute to the mechanical release of the ITAMs from the inner leaflet. Moreover, these results agree with recent simulation reports that show CD3 ITAM regulation may be controlled by the tightly coupled CD3-TCR dynamics upon pMHC binding (110–112). This hypothesis may be modified when the structure of the complete CD3 cytoplasmic domains become available on the PDB data bank (40). However, previous simulations of the CD3ε cytoplasmic tails suggest that ITAM sequestration is mediated by canonical tyrosine residues binding to negatively charged lipids (e.g., SAPI) at the liquid ordered-liquid disordered (L_o-L_d) membrane interface (113). Moreover, these results show that the CD3ε tails become more unstructured with reduced membrane interactions to liquid-ordered (L_o) membranes. Because activated T cells have L_o membranes, it is possible that upon pMHC disengagement, the lipid-lipid energy fluctuations cause the already loosened CD3ε tails to be completely released from the membrane and enable maximum ITAM phosphorylation. This work provides the impetus to attach the CD3 ITAM motifs to the CD3 coreceptor via deep learning structure generation methods (114–116) and to explore the direct effect on the membrane sequestered CD3 ITAMs upon TCR-pMHC disengagement of several TCR-pMHC pairs.

CONCLUSION

We demonstrated three central modes of action for how the CD4 coordinates with the CD3-TCR complex to hinder dissociation from the pMHC and thus potentially stimulate signal transduction and effector function. The mechanisms include the CD4 confinement of the pMHC 1.8 nm closer to the T cell membrane at equilibrium, the CD4 shift of the TCR along pMHC binding groove to strengthen the TCR-pMHC interaction by greater than 200 to 300 kJ/mol, and the stabilizing CD4 translocation that increases interaction energy between the CD4-TCR and CD4-pMHC. The shift of the TCR along the pMHC binding groove engages a different set of amino acids, and thus it has implications for the design of TCRs for immunotherapy. In addition, we find that the TCR rocks or wobbles upon pMHC dissociation and propagates energy fluctuations to the CD3-TCR, CD3-lipid, and lipid-lipid interactions. This en-

ergetic propagation may facilitate the release of CD3 ITAMs from the inner leaflet of the T cell providing a mechanotransduction-based mechanism for TCR-pMHC signal transduction. Although the generalizability to all TCR-pMHC pairs is to be determined, these results are supported by experimental observation, provide mechanistic insight on CD4-CD3-TCR trimolecular coordination, and provide impetus for future investigations on CD4-CD3-TCR/CD8 trimolecular coordination with membrane-bound CD3 ITAMs.

SUPPORTING MATERIAL

AUTHOR CONTRIBUTIONS

Z.A.R. performed the simulations, analyzed and interpreted the data, and wrote the manuscript. R.F. designed the experiments, analyzed and interpreted the data, wrote the manuscript, and secured computer time. S.C.G. designed the experiments, analyzed and interpreted the data, wrote the manuscript, and secured the funding.

ACKNOWLEDGMENTS

DECLARATION OF INTERESTS

The authors declare no competing interests.

REFERENCES

1. Mohammed, D., M. Versaevel, …, S. Gabriele. 2019. Innovative tools for mechanobiology: Unraveling outside-in and inside-out mechanotransduction. *Front. Bioeng. Biotechnol.* 7:162. https://doi.org/10.3389/FBIOE.2019.00162/BIBTEX.

2. Harrison, D. L., Y. Fang, and J. Huang. 2019. T-cell mechanobiology: Force sensation, potentiation, and translation. *Front. Phys.* 7:45. https://doi.org/10.3389/FPHY.2019.00045/BIBTEX.

3. Liu, B., E. M. Kolawole, and B. D. Evavold. 2021. Mechanobiology of T Cell Activation: To Catch a Bond. *Annu. Rev. Cell Dev. Biol.* 37:65–87. https://doi.org/10.1146/ANNUREV-CELLBIO-120219-055100.

4. Chen, W., and C. Zhu. 2013. Mechanical regulation of T-cell functions. *Immunol. Rev.* 256:160–176. https://doi.org/10.1111/imr.12122.

5. Basu, R., and M. Huse. 2017. Mechanical Communication at the Immunological Synapse. *Trends Cell Biol.* 27:241–254. https://doi.org/10.1016/j.tcb.2016.10.005.

6. Carey, S. P., A. Rahman, …, C. A. Reinhart-King. 2015. Comparative mechanisms of cancer cell migration through 3D matrix and physiological microtracks. *Am. J. Physiol. Cell Physiol.* 308:C436–C447. https://doi.org/10.1152/AJPCELL.00225.2014/ASSET/IMAGES/LARGE/ZH00051576830005.JPEG.

7. Mehta, P., Z. Rahman, …, P. E. Boukany. 2022. Microfluidics meets 3D cancer cell migration. *Trends Cancer.* 8:683–697. https://doi.org/10.1016/j.trecan.2022.03.006.

8. Ren, X., A. E. Getschman, …, F. Lin. 2021. Investigations on T cell transmigration in a human skin-on-chip (SoC) model. *Lab Chip.* 21:1527–1539. https://doi.org/10.1039/D0LC01194K.

9. Glaser, D. E., M. B. Curtis, …, S. C. George. 2022. Organ-on-a-chip model of vascularized human bone marrow niches. *Biomaterials.* 280, 121245. https://doi.org/10.1016/J.BIOMATERIALS.2021.121245.

10. Bi, Y., V. S. Shirure, …, R. C. Fields. 2020. Tumor-on-a-chip platform to interrogate the role of macrophages in tumor progression. *Integr. Biol.* 12:221–232. https://doi.org/10.1093/INTBIO/ZYAA017.

11. Göhring, J., F. Kellner, …, G. J. Schütz. 2021. Temporal analysis of T-cell receptor-imposed forces via quantitative single molecule FRET measurements. *Nat. Commun.* 121:12–14. https://doi.org/10.1038/s41467-021-22775-z.

12. Hui, K. L., L. Balagopalan, …, A. Upadhyaya. 2015. Cytoskeletal forces during signaling activation in Jurkat T-cells. *Mol. Biol. Cell.* 26:685–695. https://doi.org/10.1091/mbc.E14-03-0830.

13. Aramesh, M., S. Mergenthal, …, E. Klotzsch. 2021. Functionalized Bead Assay to Measure Three-dimensional Traction Forces during T-cell Activation. *Nano Lett.* 21:507–514. https://doi.org/10.1021/ACS.NANOLETT.0C03964/SUPPL_FILE/NL0C03964_SI_002.AVI.

14. Liu, Y., L. Blanchfield, …, K. Salaita. 2016. DNA-based nanoparticle tension sensors reveal that T-cell receptors transmit defined pN forces to their antigens for enhanced fidelity. *Proc. Natl. Acad. Sci. USA.* 113:5610–5615. https://doi.org/10.1073/pnas.1600163113.

15. Ma, R., A. V. Kellner, …, K. Salaita. 2019. DNA probes that store mechanical information reveal transient piconewton forces applied by T cells. *Proc. Natl. Acad. Sci. USA.* 116:16949–16954. https://doi.org/10.1073/pnas.1904034116.

16. Liu, B., W. Chen, …, C. Zhu. 2014. Accumulation of dynamic catch bonds between TCR and agonist peptide-MHC triggers T cell signaling. *Cell.* 157:357–368. https://doi.org/10.1016/j.cell.2014.02.053.

17. Sibener, L. V., R. A. Fernandes, …, K. C. Garcia. 2018. Isolation of a Structural Mechanism for Uncoupling T Cell Receptor Signaling from Peptide-MHC Binding. *Cell.* 174:672–687.e27. https://doi.org/10.1016/j.cell.2018.06.017.

18. Wu, P., T. Zhang, …, J. Lou. 2019. Mechano-regulation of Peptide-MHC Class I Conformations Determines TCR Antigen Recognition. *Mol. Cell.* 73:1015–1027.e7. https://doi.org/10.1016/j.molcel.2018.12.018.

19. Puech, P. H., D. Nevoltris, …, P. Bongrand. 2011. Force measurements of TCR/pMHC recognition at T cell surface. *PLoS One.* 6:e22344. https://doi.org/10.1371/JOURNAL.PONE.0022344.

20. Hu, K. H., and M. J. Butte. 2016. T cell activation requires force generation. *J. Cell Biol.* 213:535–542. https://doi.org/10.1083/JCB.201511053.

21. Das, D. K., Y. Feng, …, M. J. Lang. 2015. Force-dependent transition in the T-cell receptor β-subunit allosterically regulates peptide discrimination and pMHC bond lifetime. *Proc. Natl. Acad. Sci. USA.* 112:1517–1522. https://doi.org/10.1073/pnas.1424829112.

22. Stephens, H. M., K. N. Brazin, …, M. J. Lang. 2022. Measuring αβ T-Cell Receptor-Mediated Mechanosensing Using Optical Tweezers Combined with Fluorescence Imaging. *Methods Mol. Biol.* 2478:727–753. https://doi.org/10.1007/978-1-0716-2229-2_26.

23. Robert, P., M. Aleksic, …, P. A. Van Der Merwe. 2012. Kinetics and mechanics of two-dimensional interactions between T cell receptors and different activating ligands. *Biophys. J.* 102:248–257. https://doi.org/10.1016/j.bpj.2011.11.4018.

24. Limozin, L., M. Bridge, …, P. Robert. 2019. TCR–pMHC kinetics under force in a cell-free system show no intrinsic catch bond, but a minimal encounter duration before binding. *Proc. Natl. Acad. Sci. USA.* 116:16943–16948. https://doi.org/10.1073/pnas.1902141116.

25. Pettmann, J., L. Awada, …, P. Robert. 2022. Mechanical forces impair antigen discrimination by reducing differences in t cell receptor Off-rates. Preprint at bioRxiv. https://doi.org/10.1101/2022.05.05.490751.

26. Plattner, N., S. Doerr, …, F. Noé. 2017. Complete protein–protein association kinetics in atomic detail revealed by molecular dynamics simulations and Markov modelling. *Nat. Chem.* 9:1005–1011. https://doi.org/10.1038/nchem.2785.

27. Pan, A. C., D. Jacobson, …, D. E. Shaw. 2019. Atomic-level characterization of protein–protein association. *Proc. Natl. Acad. Sci. USA.* 116:4244–4249. https://doi.org/10.1073/PNAS.1815431116/SUPPL_FILE/PNAS.1815431116.SAPP.PDF.

28. Tomasiak, L., R. Karch, and W. Schreiner. 2022. Conformational flexibility of a free and TCR-bound pMHC-I protein investigated by long-term molecular dynamics simulations. *BMC Immunol.* 23:36. https://doi.org/10.1186/S12865-022-00510-7/FIGURES/10.

29. Rollins, Z. A., R. Faller, and S. C. George. 2022. Using Molecular Dynamics Simulations to Interrogate T Cell Receptor Non-Equilibrium Kinetics. *Comput. Struct. Biotechnol. J.* 20:2124–2133. https://doi.org/10.1016/J.CSBJ.2022.04.018.

30. Dong, D., L. Zheng, …, Z. Huang. 2019. Structural basis of assembly of the human TCR–CD3 complex. *Nature.* 573:546–552. https://doi.org/10.1038/s41586-019-1537-0.

31. Meuer, S. C., O. Acuto, …, E. L. Reinherz. 1983. Evidence for the T3-associated 90K heterodimer as the T-cell antigen receptor. *Nat.* 303:808–810. https://doi.org/10.1038/303808a0.

32. Wucherpfennig, K. W., E. Gagnon, …, M. E. Call. 2010. Structural Biology of the T-cell Receptor: Insights into Receptor Assembly, Ligand Recognition, and Initiation of Signaling. *Cold Spring Harb. Perspect. Biol.* 2, a005140. https://doi.org/10.1101/CSHPERSPECT.A005140.

33. Gaud, G., R. Lesourne, and P. E. Love. 2018. Regulatory mechanisms in T cell receptor signalling. *Nat. Rev. Immunol.* 188:485–497. https://doi.org/10.1038/s41577-018-0020-8.

34. Alcover, A., B. Alarcón, and V. Di Bartolo. 2018. Cell Biology of T Cell Receptor Expression and Regulation. *Annu. Rev. Immunol.* 36:103–125. https://doi.org/10.1146/ANNUREV-IMMUNOL-042617-053429.

35. Shah, K., A. Al-Haidari, …, J. U. Kazi. 2021. T cell receptor (TCR) signaling in health and disease. *Signal Transduct. Target. Ther.* 6:412–426. https://doi.org/10.1038/s41392-021-00823-w.

36. Kim, P. W., Z. Y. J. Sun, …, M. J. Eck. 2003. A zinc clasp structure tethers Lck to T cell coreceptors CD4 and CD8. *Science.* 301:1725–1728. https://doi.org/10.1126/SCIENCE.108563/SUPPL_FILE/KIM_PWSOM.PDF.

37. Rossy, J., D. J. Williamson, and K. Gaus. 2012. How does the kinase Lck phosphorylate the T cell receptor? Spatial organization as a regulatory mechanism. *Front. Immunol.* 3:167. https://doi.org/10.3389/FIMMU.2012.00167/BIBTEX.

38. Yin, Y., X. X. Wang, and R. A. Mariuzza. 2012. Crystal structure of a complete ternary complex of T-cell receptor, peptide-MHC, and CD4. *Proc. Natl. Acad. Sci. USA.* 109:5405–5410. https://doi.org/10.1073/PNAS.1118801109/SUPPL_FILE/PNAS.201118801SI.PDF.

39. Gao, G. F., J. Tormo, …, B. K. Jakobsen. 1997. Crystal structure of the complex between human CD8αα and HLA-A2. *Nat.* 387:630–634. https://doi.org/10.1038/42523.

40. Xu, X., H. Li, and C. Xu. 2020. Structural understanding of T cell receptor triggering. *Cell. Mol. Immunol.* 17:193–202. https://doi.org/10.1038/s41423-020-0367-1.

41. Malissen, B., and P. Bongrand. 2015. Early T Cell Activation: Integrating Biochemical, Structural, and Biophysical Cues. *Annu. Rev. Immunol.* 33:539–561. https://doi.org/10.1146/annurev-immunol-032414-112158.

42. Jiang, N., J. Huang, …, C. Zhu. 2011. Two-stage cooperative T cell receptor-peptide major histocompatibility complex-CD8 trimolecular interactions amplify antigen discrimination. *Immunity.* 34:13–23. https://doi.org/10.1016/J.IMMUNI.2010.12.017.

43. Rushdi MN, Pan V, …, Zhu C.. Cooperative binding of T cell receptor and CD4 to peptide-MHC enhances antigen sensitivity. *Nat. Commun.* 13:7055–7116. https://doi.org/10.1038/s41467-022-34587-w

44. Zech, T., C. S. Ejsing, …, T. Harder. 2009. Accumulation of raft lipids in T-cell plasma membrane domains engaged in TCR signalling. *EMBO J.* 28:466–476. https://doi.org/10.1038/EMBOJ.2009.6.

45. Yin, Y., Y. Li, …, R. A. Mariuzza. 2011. Structure of a TCR with high affinity for self-antigen reveals basis for escape from negative selection. *EMBO J.* 30:1137–1148. https://doi.org/10.1038/EMBOJ.2011.21.

46. Wittlich, M., P. Thiagarajan, …, D. Willbold. 2010. NMR structure of the transmembrane and cytoplasmic domains of human CD4 in micelles. *Biochim. Biophys. Acta.* 1798:122–127. https://doi.org/10.1016/J.BBAMEM.2009.09.010.

47. Shen, M.-Y., and A. Sali. 2006. Statistical potential for assessment and prediction of protein structures. *Protein Sci.* 15:2507–2524. https://doi.org/10.1110/ps.062416606.

48. Fiser, A. S., and A. S. Ali. 2003. Homology-Based Protein Structure Models. http://salilab.org/.

49. Webb, B., and A. Sali. 2016. Comparative Protein Structure Modeling Using MODELLER. *Curr Protoc Bioinforma.* 54:5.6.1–5.6.37. https://doi.org/10.1002/CPBI.3.

50. Cochran, J. R., T. O. Cameron, and L. J. Stern. 2000. The relationship of MHC-peptide binding and T cell activation probed using chemically defined MHC class II oligomers. *Immunity.* 12:241–250. https://doi.org/10.1016/S1074-7613(00)80177-6.

51. Ge, Q., J. D. Stone, …, L. J. Stern. 2002. Soluble peptide-MHC monomers cause activation of CD8+ T cells through transfer of the peptide to T cell MHC molecules. *Proc. Natl. Acad. Sci. USA.* 99:13729–13734. https://doi.org/10.1073/PNAS.212515299/SUPPL_FILE/5152FIG9.JPG.

52. Sušac, L., M. T. Vuong, …, S. J. Davis. 2022. Structure of a fully assembled tumor-specific T cell receptor ligated by pMHC. *Cell.* 185:3201–3213.e19. https://doi.org/10.1016/j.cell.2022.07.010.

53. Chen, Y., Y. Zhu, …, Z. Huang. 2022. Cholesterol inhibits TCR signaling by directly restricting TCR-CD3 core tunnel motility. *Mol. Cell.* 82:1278–1287.e5. https://doi.org/10.1016/J.MOLCEL.2022.02.017.

54. Jo, S., T. Kim, …, W. Im. 2008. CHARMM-GUI: A web-based graphical user interface for CHARMM. *J. Comput. Chem.* 29:1859–1865. https://doi.org/10.1002/JCC.20945.

55. Jo, S., X. Cheng, …, W. Im. 2014. CHARMM-GUI PDB manipulator for advanced modeling and simulations of proteins containing nonstandard residues. *Adv. Protein Chem. Struct. Biol.* 96:235–265. https://doi.org/10.1016/BS.APCSB.2014.06.002.

56. Park, S. J., N. Kern, …, W. Im. 2023. CHARMM-GUI PDB Manipulator: Various PDB Structural Modifications for Biomolecular Modeling and Simulation. *J. Mol. Biol.*167995 https://doi.org/10.1016/J.JMB.2023.167995.

57. Wu, E. L., X. Cheng, …, W. Im. 2014. CHARMM-GUI Membrane Builder toward realistic biological membrane simulations. *J. Comput. Chem.* 35:1997–2004. https://doi.org/10.1002/JCC.23702.

58. Jo, S., J. B. Lim, …, W. Im. 2009. CHARMM-GUI membrane builder for mixed bilayers and its application to yeast membranes. *Biophys. J.* 97:50–58. https://doi.org/10.1016/j.bpj.2009.04.013.

59. Jo, S., T. Kim, and W. Im. 2007. Automated Builder and Database of Protein/Membrane Complexes for Molecular Dynamics Simulations. *PLoS One.* 2, e880. https://doi.org/10.1371/JOURNAL.PONE.0000880.

60. Lee, J., D. S. Patel, …, W. Im. 2019. CHARMM-GUI Membrane Builder for Complex Biological Membrane Simulations with Glycolipids and Lipoglycans. *J. Chem. Theory Comput.* 15:775–786. https://doi.org/10.1021/ACS.JCTC.8B01066/SUPPL_FILE/CT8B01066_SI_001.PDF.

61. Miguel, L., D. M. Owen, …, E. C. Jury. 2011. Primary human CD4+ T cells have diverse levels of membrane lipid order that correlate with their function. *J. Immunol.* 186:3505–3516. https://doi.org/10.4049/JIMMUNOL.1002980.

62. Börtlein, C., A. Draeger, …, E. Avota. 2018. The neutral sphingomyelinase 2 is required to polarize and sustain T cell receptor signaling. *Front. Immunol.* 9, 347324. https://doi.org/10.3389/FIMMU.2018.00815/BIBTEX.

63. Börtlein, C., F. Schumacher, …, E. Avota. 2019. Role of neutral sphingomyelinase-2 (Nsm 2) in the control of t cell plasma membrane lipid composition and cholesterol homeostasis. *Front. Cell Dev. Biol.* 7:1–16. https://doi.org/10.3389/FCELL.2019.00226/BIBTEX.

64. Hose, M., A. Günther, …, W. Hansen. 2022. Cell-intrinsic ceramides determine T cell function during melanoma progression. *Elife.* 11:e83073. https://doi.org/10.7554/ELIFE.83073.

65. Verheugen, J. A., H. P. Vijverberg, …, M. D. Cahalan. 1995. Voltage-gated and Ca(2+)-activated K+ channels in intact human T lymphocytes. Noninvasive measurements of membrane currents, membrane potential, and intracellular calcium. *J. Gen. Physiol.* 105:765–794. https://doi.org/10.1085/JGP.105.6.765.

66. Papp, F., P. Hajdu, …, G. Panyi. 2020. Periodic Membrane Potential and Ca2+ Oscillations in T Cells Forming an Immune Synapse. *Int. J. Mol. Sci.* 21:1568. https://doi.org/10.3390/IJMS21051568.

67. Brooks, B. R., C. L. Brooks, …, M. Karplus. 2009. CHARMM: The biomolecular simulation program. *J. Comput. Chem.* 30:1545–1614. https://doi.org/10.1002/JCC.21287.

68. Lee, J., X. Cheng, …, I. Wonphil. 2016. CHARMM-GUI Input Generator for NAMD, GROMACS, AMBER, OpenMM, and CHARMM/OpenMM Simulations Using the CHARMM36 Additive Force Field. *J. Chem. Theor. Comput.* 12:405–413. https://doi.org/10.1021/ACS.JCTC.5B00935/ASSET/IMAGES/LARGE/CT-2015-00935E_0005.JPEG.

69. Abraham, M. J., T. Murtola, …, E. Lindahl. 2015. Gromacs: High performance molecular simulations through multi-level parallelism from laptops to supercomputers. *SoftwareX.* 1-2:19–25. https://doi.org/10.1016/J.SOFTX.2015.06.001.

70. Van Der Spoel, D., E. Lindahl, …, H. J. C. Berendsen. 2005. GROMACS: Fast, flexible, and free. *J. Comput. Chem.* 26:1701–1718. https://doi.org/10.1002/jcc.20291.

71. Evans, D. J., and B. L. Holian. 1985. The Nose–Hoover thermostat. *J. Chem. Phys.* 83:4069–4074.

72. Parrinello, M., and A. Rahman. 1981. Polymorphic transitions in single crystals: A new molecular dynamics method. *J. Appl. Phys.* 52:7182–7190. https://doi.org/10.1063/1.328693.

73. Ewald, P. P. 1921. Die Berechnung optischer und elektrostatischer Gitterpotentiale. *Ann. Phys.* 369:253–287. https://doi.org/10.1002/andp.19213690304.

74. Di Pierro, M., R. Elber, and B. Leimkuhler. 2015. A Stochastic Algorithm for the Isobaric-Isothermal Ensemble with Ewald Summations for All Long Range Forces. *J. Chem. Theory Comput.* 11:5624–5637. https://doi.org/10.1021/acs.jctc.5b00648.

75. Hess, B., H. Bekker, …, J. G. E. M. Fraaije. 1997. LINCS: A Linear Constraint Solver for molecular simulations. *J. Comput. Chem.* 18:1463–1472.

76. Miyamoto, S., and P. A. Kollman. 1992. Settle: An analytical version of the SHAKE and RATTLE algorithm for rigid water models. *J. Comput. Chem.* 13:952–962. https://doi.org/10.1002/JCC.540130805.

77. Chodera, J. D. 2016. A Simple Method for Automated Equilibration Detection in Molecular Simulations. *J. Chem. Theor. Comput.* 12:1799–1805. https://doi.org/10.1021/ACS.JCTC.5B00784/ASSET/IMAGES/MEDIUM/CT-2015-00784B_0007.GIF.

78. Knapp, B., L. Ospina, and C. M. Deane. 2018. Avoiding False Positive Conclusions in Molecular Simulation: The Importance of Replicas. *J. Chem. Theory Comput.* 14:6127–6138. https://doi.org/10.1021/acs.jctc.8b00391.

79. Rollins, Z. A., J. Huang, …, S. C. George. 2022. A computational algorithm to assess the physiochemical determinants of T cell receptor dissociation kinetics. *Comput. Struct. Biotechnol. J.* 20:3473–3481. https://doi.org/10.1016/J.CSBJ.2022.06.048.

80. Rollins, Z., B. Harris, …, R. Faller. 2022. A molecular dynamics investigation of N-glycosylation effects on T-cell receptor kinetics. *J. Biomol. Struct. Dyn.* 1–10. https://doi.org/10.1080/07391102.2022.2091660.

81. Rollins, Z. A., M. B. Curtis, …, S. C. George. 2022. Automated protein-protein structure prediction of the T cell receptor-peptide major histocompatibility complex. Preprint at bioRxiv. https://doi.org/10.1101/2022.06.01.494331.

82. Sieradzan, A. K., and R. Jakubowski. 2017. Introduction of steered molecular dynamics into UNRES coarse-grained simulations package. *J. Comput. Chem.* 38:553–562. https://doi.org/10.1002/JCC.24685.

83. Kim, S. T., K. Takeuchi, …, E. L. Reinherz. 2009. The αβ T cell receptor is an anisotropic mechanosensor. *J. Biol. Chem.* 284:31028–31037. https://doi.org/10.1074/jbc.M109.052712.

84. Polacheck, W. J., and C. S. Chen. 2016. Measuring cell-generated forces: a guide to the available tools. *Nat. Methods.* 13:415–423. https://doi.org/10.1038/nmeth.3834.

85. Harris, C. R., K. J. Millman, …, T. E. Oliphant. 2020. Array programming with NumPy. *Nat.* 585:357–362. https://doi.org/10.1038/s41586-020-2649-2.

86. Mckinney, W. 2010. Data Structures for Statistical Computing in Python.

87. Hunter, J. D., and D. J. Hunter. 2007. Matplotlib: A 2D Graphics Environment. *CSE.* 9:90–95. https://doi.org/10.1109/MCSE.2007.55.

88. Beckstein O. GromacsWrapper.Preprint at. Zendo. doi:10.5281/zenodo.17901

89. Virtanen, P., R. Gommers; …, SciPy 1.0 Contributors. 2020. SciPy 1.0: fundamental algorithms for scientific computing in Python. *Nat. Methods.* 17:261–272. https://doi.org/10.1038/s41592-019-0686-2.

90. Vallat, R. 2018. Pingouin: statistics in Python. *J. Open Source Softw.* 3:1026. https://doi.org/10.21105/JOSS.01026.

91. Michaud-Agrawal, N., E. J. Denning, …, O. Beckstein. 2011. MDAnalysis: A toolkit for the analysis of molecular dynamics simulations. *J. Comput. Chem.* 32:2319–2327. https://doi.org/10.1002/jcc.21787.

92. Gowers R, Linke M, …, Oliver, B. MDAnalysis: A python package for the rapid analysis of molecular dynamics simulations. in Proceedings of the 15th Python in Science Conference. https://doi.org/10.25080/majora-629e541a-00e

93. Buchoux, S. 2017. FATSLiM: a fast and robust software to analyze MD simulations of membranes. *Bioinformatics.* 33:133–134. https://doi.org/10.1093/BIOINFORMATICS/BTW563.

94. Smith, P., and C. D. Lorenz. 2021. LiPyphilic: A Python Toolkit for the Analysis of Lipid Membrane Simulations. *J. Chem. Theor. Comput.* 17:5907–5919. https://doi.org/10.1021/ACS.JCTC.1C00447/SUPPL_FILE/CT1C00447_SI_001.PDF.

95. Skaug, M. J., M. L. Longo, and R. Faller. 2011. The impact of texas red on lipid bilayer properties. *J. Phys. Chem. B.* 115:8500–8505. https://doi.org/10.1021/JP203738M/ASSET/IMAGES/MEDIUM/JP-2011-03738M_0010.GIF.

96. Faller, R. 2016. Molecular modeling of lipid probes and their influence on the membrane. *Biochim. Biophys. Acta.* 1858:2353–2361. https://doi.org/10.1016/J.BBAMEM.2016.02.014.

97. Kemmerer, S., J. C. Voss, and R. Faller. 2013. Molecular dynamics simulation of dipalmitoylphosphatidylcholine modified with a MTSL nitroxide spin label in a lipid membrane. *Biochim. Biophys. Acta.* 1828:2770–2777. https://doi.org/10.1016/J.BBAMEM.2013.07.030.

98. Kheyfets, B. B., and S. I. Mukhin. 2015. Area Per Lipid in DPPC-Cholesterol Bilayers:Analytical Approach. https://arxiv.org/abs/1501.02727v1.

99. Baker, M. K., and C. F. Abrams. 2014. Dynamics of lipids, cholesterol, and transmembrane α-helices from microsecond molecular dynamics simulations. *J. Phys. Chem. B.* 118:13590–13600. https://doi.org/10.1021/JP507027T/SUPPL_FILE/JP507027T_SI_001.PDF.

100. Saeedimasine, M., A. Montanino, …, A. Villa. 2019. Role of lipid composition on the structural and mechanical features of axonal membranes: a molecular simulation study. *Sci. Rep.* 9:8000–8001. https://doi.org/10.1038/s41598-019-44318-9.

101. MacDermaid, C. M., H. K. Kashyap, …, G. Fiorin. 2015. Molecular dynamics simulations of cholesterol-rich membranes using a coarse-grained force field for cyclic alkanes. *J. Chem. Phys.* 143, 243144. https://doi.org/10.1063/1.4937153.

102. Howie, D., A. Ten Bokum, …, H. Waldmann. 2017. The role of lipid metabolism in T lymphocyte differentiation and survival. *Front. Immunol.* 8:1949. https://doi.org/10.3389/FIMMU.2017.01949/BIBTEX.

103. Subczynski, W. K., M. Pasenkiewicz-Gierula, …, M. Raguz. 2017. High cholesterol/low cholesterol: Effects in biological membranes Review. *Cell Biochem. Biophys.* 75:369–385. https://doi.org/10.1007/S12013-017-0792-7.

104. Filippov, A., G. Orädd, and G. Lindblom. 2003. The Effect of Cholesterol on the Lateral Diffusion of Phospholipids in Oriented Bilayers. *Biophys. J.* 84:3079–3086. https://doi.org/10.1016/S0006-3495(03)70033-2.

105. Carpenter, E. P., K. Beis, …, S. Iwata. 2008. Overcoming the challenges of membrane protein crystallography. *Curr. Opin. Struct. Biol.* 18:581–586. https://doi.org/10.1016/J.SBI.2008.07.001.

106. Bagheri, Y., A. A. Ali, and M. You. 2020. Current Methods for Detecting Cell Membrane Transient Interactions. *Front. Chem.* 8:1074. https://doi.org/10.3389/FCHEM.2020.603259/BIBTEX.

107. Lindahl, E., and M. S. P. Sansom. 2008. Membrane proteins: molecular dynamics simulations. *Curr. Opin. Struct. Biol.* 18:425–431. https://doi.org/10.1016/J.SBI.2008.02.003.

108. Goossens, K., and H. De Winter. 2018. Molecular Dynamics Simulations of Membrane Proteins: An Overview. *J. Chem. Inf. Model.* 58:2193–2202. https://doi.org/10.1021/ACS.JCIM.8B00639/ASSET/IMAGES/MEDIUM/CI-2018-00639C_0005.GIF.

109. Stansfeld, P. J., and M. S. P. Sansom. 2011. Molecular Simulation Approaches to Membrane Proteins. *Structure.* 19:1562–1572. https://doi.org/10.1016/J.STR.2011.10.002.

110. Alba, J., and M. D'abramo. 2022. The Full Model of the pMHC-TCR-CD3 Complex: A Structural and Dynamical Characterization of Bound and Unbound States. *Cells.* 11:668. https://doi.org/10.3390/CELLS11040668/S1.

111. van Eerden, F. J., A. Alrahman Sherif, …, D. Standley. 2023. TCR-pMHC complex formation triggers CD3 dynamics. Preprint at bioRxiv. https://doi.org/10.1101/2022.07.27.501668.

112. Prakaash, D., G. P. Cook, …, A. C. Kalli. 2021. Multi-scale simulations of the T cell receptor reveal its lipid interactions, dynamics and the arrangement of its cytoplasmic region. *PLoS Comput. Biol.* 17, e1009232. https://doi.org/10.1371/JOURNAL.PCBI.1009232.

113. López, C. A., A. Sethi, …, S. Gnanakaran. 2015. Membrane-Mediated Regulation of the Intrinsically Disordered CD3ε Cytoplasmic Tail of the TCR. *Biophys. J.* 108:2481–2491. https://doi.org/10.1016/j.bpj.2015.03.059.

114. Jumper, J., R. Evans, …, D. Hassabis. 2021. Highly accurate protein structure prediction with AlphaFold. *Nat.* 596:583–589. https://doi.org/10.1038/s41586-021-03819-2.

115. Evans, R., M. O'Neill, …, D. Hassabis. 2021. Protein complex prediction with AlphaFold-Multimer. Preprint at bioRxiv. https://doi.org/10.1101/2021.10.04.463034.

116. Mirdita, M., K. Schütze, …, M. Steinegger. 2022. ColabFold - Making protein folding accessible to all. Preprint at bioRxiv. https://doi.org/10.1101/2021.08.15.456425.